

NGC 300 ULX1: spin evolution, super-Eddington accretion, and outflows

G. Vasilopoulos¹,^{*} M. Petropoulou², F. Koliopoulos³, P. S. Ray⁴, C. B. Bailyn¹,
F. Haberl⁵ and K. Gendreau⁶

¹Department of Astronomy, Yale University, PO Box 208101, New Haven, CT 06520-8101, USA

²Department of Astrophysical Sciences, Princeton University, 4 Ivy Lane, Princeton, NJ 08544, USA

³IRAP, CNRS, 9 avenue du Colonel Roche, BP 44346, F-31028 Toulouse Cedex 4, France

⁴Space Science Division, U.S. Naval Research Laboratory, Washington, DC 20375, USA

⁵Max-Planck-Institut für Extraterrestrische Physik, Giessenbachstraße, 85748 Garching, Germany

⁶X-Ray Astrophysics Laboratory, NASA Goddard Space Flight Center, Greenbelt, MD 20771, USA

Accepted 2019 July 21. Received 2019 July 1; in original form 2019 April 28

ABSTRACT

NGC 300 ULX1 is an ultraluminous X-ray pulsar, showing an unprecedented spin evolution, from about 126 s to less than 20 s in only 4 yr, consistent with steady mass accretion rate. Following its discovery we have been monitoring the system with *Swift* and *NICER* to further study its properties. We found that even though the observed flux of the system dropped by a factor of $\gtrsim 20$, the spin-up rate remained almost constant. A possible explanation is that the decrease in the observed flux is a result of increased absorption of obscuring material due to outflows or a precessing accretion disc.

Key words: stars: neutron – pulsars: individual: NGC 300 ULX1 – galaxies: individual: NGC 300 – X-rays: binaries.

1 INTRODUCTION

Ultraluminous X-ray sources (ULXs) are binary systems that emit radiation in excess of the Eddington limit as computed for accretion onto a stellar-mass compact object (Kaaret, Feng & Roberts 2017). Although super-Eddington mass transfer rates have been postulated for ULX systems (hosting black-holes; e.g. King et al. 2001), the first undisputed evidence was provided by the discovery of the first ultraluminous X-ray pulsar (ULXP) M82 X-2 (Bachetti et al. 2014). In addition, it has been shown that the X-ray spectral properties of pulsating and non-pulsating ULXs are consistent with a neutron star (NS) being the central engine (Koliopoulos et al. 2017) and accreting at super-Eddington rates.

Given the super-Eddington mass accretion rates in ULXPs, it is expected that a fraction of the total accreted mass will be lost through outflows, launched from the inner accretion disc (Shakura & Sunyaev 1973). These outflows can be optically thick to the X-ray radiation produced by the NS, thus creating an obscuring envelope around it (Poutanen et al. 2007). However, the outflows are not spherical and X-ray radiation can still escape from a central hollow cone region (King, Lasota & Kluźniak 2017; King & Lasota 2019).

For three of the known ULXPs, orbital periods have been derived from pulsar timing, while super-orbital periodicities have been evident in their X-ray light curves (e.g. Kaaret, Simet & Lang 2006; Motch et al. 2014). M82 X-2 has an orbital period of ~ 2.5 d and a ~ 64 d super-orbital period (Bachetti et al. 2014; Brightman et al. 2019). NGC 5907 ULX1 has a 5.3 d and 78 d orbital and

super-orbital period, respectively (Israel et al. (Fürst et al. 2017; Israel et al. 2017). NGC 7793 P13 has an orbital period of ~ 64 d, while its X-ray light-curve has a ~ 67 d superorbital periodicity (e.g. Fürst et al. 2018). The observed X-ray flux (F_X) during these super-orbital phases can vary by a factor of 100, with no evidence of spectral changes expected from accretor-to-propeller transitions (Illarionov & Sunyaev 1975; Corbet 1996; Campana et al. 2018). A possible scenario to explain the flux changes on superorbital time-scales is the obscuration from a precessing accretion disc (Fürst et al. 2017; Middleton et al. 2018). However, the latter has never been confirmed by any timing study of their pulse period evolution.

NGC 300 ULX1 is a recently discovered ULXP (Carpano et al. 2018), located at a distance of 1.88 Mpc (Gieren et al. 2005). The system was classified as a supernova impostor, after it became active in 2010 (SN 2010da; Binder et al. 2011). Its ULXP classification was based on the analysis of data obtained by simultaneous *XMM-Newton* and *NuSTAR* observations in 2016 December, which yielded a spin period (P) of ~ 31 s and an unabsorbed X-ray luminosity (in the 0.3–30 keV band) $L_X \sim 4.7 \times 10^{39}$ erg s⁻¹ (Carpano et al. 2018). Analysis of the X-ray spectra of NGC 300 ULX1 has shown that its intrinsic X-ray luminosity between 2010 and early 2018 remained constant (within a factor of ~ 3), with any large changes in its observed flux being attributed to a variable absorption component (Carpano et al. 2018; Vasilopoulos et al. 2018; Koliopoulos et al. 2019). Analysis of archival X-ray data revealed a remarkable spin up of the NS, whose spin period changed from ~ 126 to ~ 19 s between 2014 November and 2018 April (Vasilopoulos et al. 2018). Further X-ray monitoring of NGC 300 ULX1 during the first half of 2018 with *NICER* revealed only small changes in the observed F_X and confirmed a constant spin-up rate (Ray et al. 2018).

* E-mail: georgios.vasilopoulos@yale.edu

In this work, we study the evolution of NGC 300 ULX1 using X-ray monitoring observations that cover the time period between 2018 August and December. We show that the observed X-ray flux of NGC 300 ULX1 dropped by a factor of $\gtrsim 20$ –30 from its peak value in 2018, but the NS spin-up rate remained roughly constant (Section 2). The latter requires a constant accretion rate, and thus a steady energy release (i.e. intrinsic L_X) assuming the radiative efficiency remains the same. Our results can be understood in the context of super-Eddington accretion onto a magnetized NS (Section 3), with the required absorption being caused by either obscuration from a precessing accretion disc or mass outflows launched from the inner parts of the disc due to very high accretion rates (Section 4).

2 X-RAY MONITORING OBSERVATIONS

Our findings are based on *Swift*/XRT and *NICER* observations of NGC 300 ULX1 that were obtained mainly in 2018. Between 2018 January and July the X-ray flux of NGC 300 ULX1 gradually declined by a factor of ~ 2 , but still remained at a super-Eddington level (Ray et al. 2018). In 2018 August–September the observed F_X rapidly declined and the system was no longer visible with either *NICER* or *Swift*/XRT. The latest spin period measurement, on 2018 August 21, yielded $P = 17.52 \pm 0.04$ s.

In 2018 November, *Swift*/XRT monitoring observations (PI: Kennea, J) indicated a rebrightening of the system. We thus requested *NICER* target of opportunity (ToO) observations (PI: Vasilopoulos, G) to measure the NS’s pulse period. *NICER* measured a spin period of 16.58 ± 0.04 s on 2019 November 28 (MJD 58451), revealing a spin change of ~ 1 s within ~ 100 d.

2.1 Data analysis

We used *Swift*/XRT to measure the X-ray flux of NGC 300 ULX1. *Swift*/XRT data products are available through the UK *Swift* science data centre¹ (Evans et al. 2007, 2009).

Basic information about spectral changes of the observed spectrum can be derived from the hardness ratio (HR). This is defined as the ratio of the difference over the sum of the number of counts in two subsequent energy bands: $HR = (R_{i+1} - R_i)/(R_{i+1} + R_i)$, where R_i is the background-subtracted count rate in a specific energy band.

We used data obtained by *NICER* from 2018 February 6 through 2019 February 4 to obtain accurate measurements of the spin frequency evolution of NGC 300 ULX1. We followed the maximum likelihood procedure described by Ray et al. (2018) on segments of data with gaps less than 1000 s and spanning no more than 3000 s. The points plotted in Fig. 1 are the detections where the data span at least 360 s with a significance of at least 4.5σ .

2.2 Results

Carpano et al. (2018) found that the multiepoch broadband spectra of NGC 300 ULX1 are best fitted by a multicomponent continuum, where the spectrum can be phenomenologically described by a power law ($\Gamma \sim 1.5$) with cut-off ($E_{\text{cut}} \sim 6.6$ keV, $E_{\text{fold}} \sim 4.8$ keV), with a soft excess (i.e. below 1.0 keV) attributed to a black body component ($kT \sim 0.17$ keV). Most importantly, the authors showed that the spectral continuum is partially absorbed

by material with high column density, showing no clear low-energy cut-off but a rather complicated spectral shape (see also Koliopoulos et al. 2019). The *Swift*/XRT data do not provide enough statistics for a detailed spectral fit and, as a result, we cannot constrain the partial absorption component. Thus, for the conversion of *Swift*/XRT count rates to F_X (0.3–30.0 keV) we used the spectral properties derived by Carpano et al. (2018) for the continuum spectrum, a constant absorption (accounting only for Galactic absorption), and assumed distance of 1.88 Mpc. In other words, the derived X-ray light curve, shown in Fig. 1, is not corrected for the intrinsic absorption of the system.² Within the period 2018 August–November (see grey shaded area in Fig. 1; MJD ~ 58350 –58450), the observed F_X of NGC 300 ULX1 rapidly decreased. As already noted, due to the limited statistics we can put no constraints on the spectral change that accompanied this transition.

Prior to this work, Vasilopoulos et al. (2018) have investigated the spin evolution of NGC 300 ULX1 by analysing archival X-ray data and searching for periodic signals using the accelerated epoch-folding method (Leahy et al. 1983). Both P and \dot{P} were measured, with small uncertainties, for three epochs where *XMM-Newton*, *Chandra*, and *NuSTAR* data with high statistics were available. The derived values of $\dot{\nu}$ are 5.5×10^{-10} , 4.5×10^{-10} , and 3.8×10^{-10} s⁻² (Vasilopoulos et al. 2018). We used *NICER* monitoring data to extend these measurements. During 2018 the evolution of the NS spin frequency follows an almost linear trend with time (see bottom panel in Fig. 1). To derive precise period measurements, we employed a maximum likelihood technique to measure pulsed frequencies and their significance (see details Ray et al. 2011, 2018). For this purpose, we only used ‘good’ detections.³ We fitted the time-series of the NS frequencies with a Bayesian approach to linear regression (Kelly 2007) and derived a slope of $(4.031 \pm 0.026) \times 10^{-10}$ s⁻² (90 per cent confidence level). When fitting the data with a polynomial model instead, we derive an ephemeris with $\nu = 0.053347 \pm 0.000003$ s⁻¹, $\dot{\nu} = (4.23 \pm 0.03) \times 10^{-10}$ s⁻², and $\ddot{\nu} = (4.4 \pm 0.5) \times 10^{-18}$ s⁻³ at epoch MJD 58243.515. The secular frequency evolution as derived above is in agreement (~ 20 per cent deviation) with the instantaneous $\dot{\nu}$ measured by Carpano et al. (2018) and Vasilopoulos et al. (2018).

In the following section, we show that the spin evolution of the NS in NGC 300 ULX1 during 2018 requires a roughly constant accretion rate in excess of the Eddington limit ($\sim 2 \times 10^{18}$ g s⁻¹), whereas the light curve clearly shows a decrease of the observed F_X . This controversy can be naturally resolved, if one attributes the decay of the observed F_X to an increased absorption due to extra material present in the line of sight. The absorbing material can be the result of outflows launched from the accretion disc and/or of the disc precession.

3 ACCRETION AND TORQUES IN ULX PULSARS

The Eddington luminosity of an accreting object is obtained by equating the outward radiation pressure with the gravitational

²In this context the observed flux F_X , plotted in Fig. 1, when corrected for the distance modulus of NGC 300, is the L_X .

³These have likelihood test statistic less than 21, span of observation greater than 360 s, and more than 70 per cent of good exposure time within that span (see also Ray et al. 2018).

¹http://www.swift.ac.uk/user_objects/

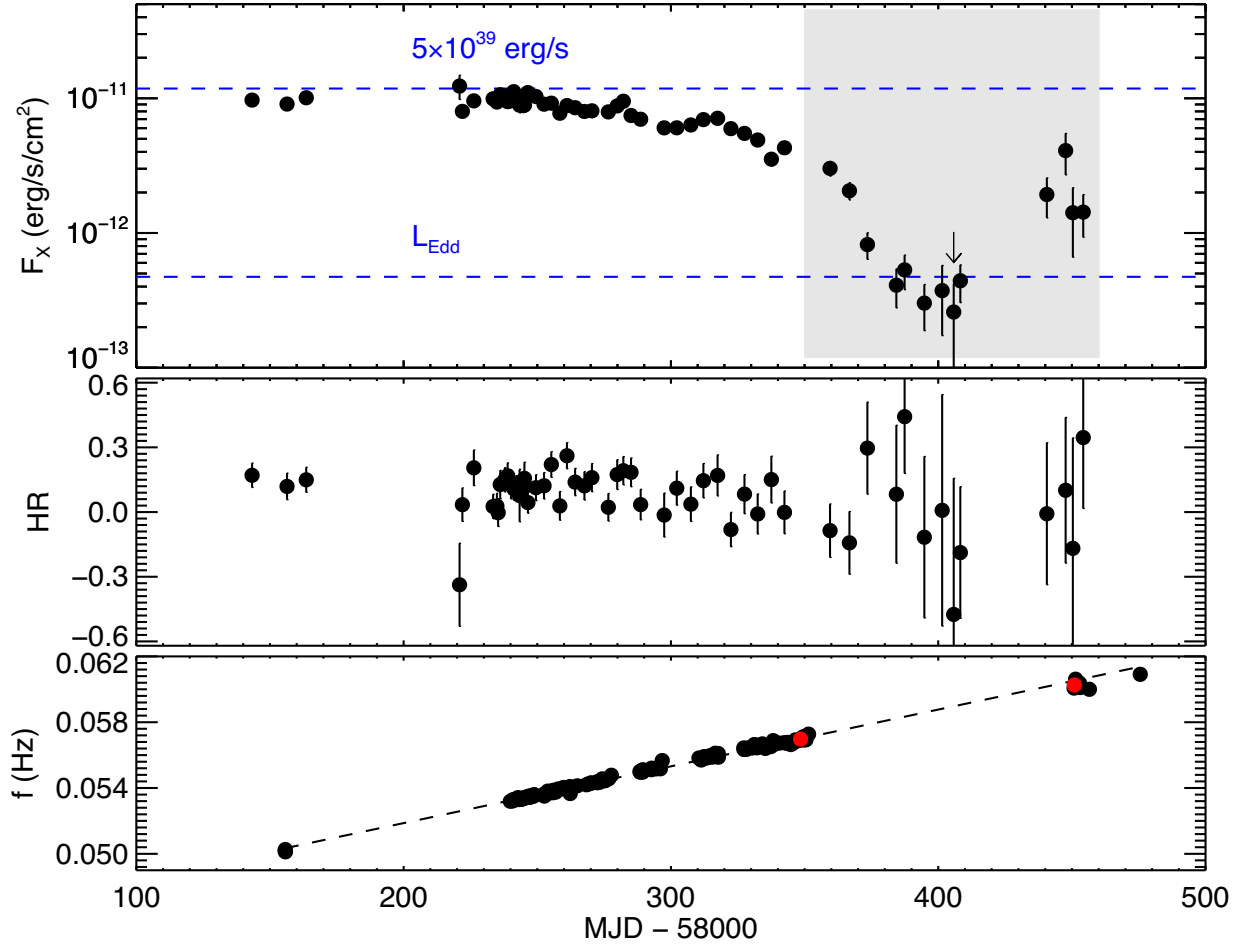


Figure 1. Top panel: X-ray light-curve (0.3–30 keV band) of NGC 300 ULX1 as derived from *Swift*/XRT observations (black points) performed within 2018. We used the spectral properties derived by Carpano et al. (2018), assuming a constant absorption, to convert *Swift*/XRT count rates to F_X (see the text). Horizontal dashed blue lines mark characteristic luminosity levels converted to expected flux for a distance of 1.88 Mpc. The shaded area indicates the period of the rapid X-ray flux decline and recovery discussed in the text. Middle panel: temporal evolution of the hardness ratio (HR) as derived from the soft (0.3–1.5 keV) and hard (1.5–10.0 keV) energy bands. Bottom panel: temporal evolution of the measured spin frequencies derived from *NICER* observations (see Ray et al. 2018). The black dashed line denotes the best linear fit to the data, which yields $\dot{M} = 2.3 \times 10^{19} \text{ g s}^{-1}$ (see the text for details; Section 3.1). The red points are the *NICER* detections with the highest significance (see Ray et al. 2018, for details) just before the decay and after the rise of the F_X .

force:

$$L_{\text{Edd}} = \frac{4\pi GM_{\text{NS}}c}{\kappa} \approx 1.5 \times 10^{38} m_1 \text{ erg s}^{-1}, \quad (1)$$

where G is the gravitational constant, $\kappa = 0.2(1 + X) \text{ cm}^2 \text{ g}^{-1}$ is the Thomson opacity, X is the hydrogen mass fraction for solar abundances ($X = 0.7$), and $m_1 \equiv M_{\text{NS}}/M_{\odot}$ is the NS mass (in units of the solar mass).

At low mass accretion rates, the disc is locally sub-Eddington and its inner part is gas-pressure-dominated (regime 1). For mass accretion rates exceeding the critical rate \dot{M}_{Edd} :

$$\dot{M}_{\text{Edd}} = \frac{48\pi GM_{\text{NS}}}{c\kappa} \simeq 2 \times 10^{18} m_1 \text{ g s}^{-1}, \quad (2)$$

part of the dissipated energy is used to launch mass outflows from the inner part of the accretion disc, thus leading to a reduced accretion rate onto the compact object. This occurs inside the spherization radius R_{sph} , where the disc thickness becomes comparable to its radius (Shakura & Sunyaev 1973) or, equivalently, the disc luminosity becomes equal to L_{Edd} (see equation 18 in Poutanen

et al. 2007):

$$R_{\text{sph}} \approx 10 \frac{GM_{\text{NS}}\dot{m}_0}{c^2} \simeq 15 m_1 \dot{m}_0 \text{ km}, \quad (3)$$

where \dot{m}_0 is the mass accretion rate at R_{sph} in units of \dot{M}_{Edd} . In this regime, the outflows launched from within the spherization radius are reconfiguring accretion in a way that the local disc accretion rate is sub-Eddington (Shakura & Sunyaev 1973). In the classical mass-loss model of Shakura & Sunyaev (1973), the mass accretion rate at $R < R_{\text{sph}}$ can be written as:

$$\dot{M}(R) \simeq \frac{R}{R_{\text{sph}}} \dot{m}_0 \dot{M}_{\text{Edd}}. \quad (4)$$

This is only an approximate relation, as it does not take into account the effects of heat advection in the disc. Inclusion of the latter results in a more gradual decrease of \dot{M} with radius than the one dictated by equation (4) (Poutanen et al. 2007; Chashkina et al. 2019; Mushtukov et al. 2019).

In contrast to non-magnetized accreting objects, the accretion discs around magnetized NSs do not extend to the innermost stable orbit, but they are truncated at much larger radii due to the interaction

with the NS magnetic field. The magnetospheric radius provides an estimate of the disc inner radius (Ghosh, Lamb & Pethick 1977):

$$R_M = \xi \left(\frac{R_{\text{NS}}^{12} B^4}{2GM_{\text{NS}} \dot{M}^2} \right)^{1/7}, \quad (5)$$

where R_{NS} is the neutron star radius and $\xi \sim 0.5$ (Campana et al. 2018). For typical B values in X-ray pulsars (e.g. 10^{12} G), very high mass accretion rates are required (e.g. $\dot{m}_0 > 10$) to make $R_{\text{sph}} > R_M$ (regime 2).

Although heat advection is operating in the disc even at sub-Eddington rates, where no outflows are present, it begins to play an increasingly important role in the energy balance of the inner disc at super-Eddington rates, i.e. $\dot{m}_0 \gtrsim 20$ (regime 3) and eventually becomes the dominant process at extremely high rates, i.e. $\dot{m}_0 \gtrsim 100$ for typical X-ray pulsar magnetic fields (see fig. 12 of Chashkina et al. 2019).⁴ Because of the heat advection, the radiation energy flux transported by diffusion in the vertical direction is less than the one released locally in the disc (Mushtukov et al. 2019). The advection process effectively leads to a reduced mass-loss from the disc. The outflow rate in this regime is a constant fraction of the mass accretion rate at R_{sph} and cannot exceed ~ 50 per cent – 60 per cent (see e.g. fig. 3 in Mushtukov et al. 2019).

In what follows, we interpret our findings (see Fig. 1 and Section 2.2) in the context of the three regimes described above and schematically shown in Fig. 2.

3.1 Spin-evolution without outflows

The spin evolution of a sub-Eddington accreting NS can be theoretically predicted, if two parameters are known, the accretion rate and the surface magnetic field of the NS (Wang 1995). In X-ray pulsars, material is deposited onto the magnetic pole of the NS, forming the so-called accretion column (e.g. Becker & Wolff 2007; Mushtukov et al. 2015). The bolometric X-ray luminosity of the system, which originates from the accretion column, can be converted to a mass accretion rate \dot{M} assuming some efficiency η_{eff} (i.e. $L_X \approx \eta_{\text{eff}} \dot{M} c^2$). This is generally assumed to be the efficiency with which gravitational energy is converted to radiation, namely $L_X = GM_{\text{NS}} \dot{M} / R$. For $R = R_{\text{NS}} = 10^6$ cm and $M_{\text{NS}} = 1.4M_{\odot}$, one finds $L_X \approx 0.2 \dot{M} c^2$. Henceforth, we adopt $\eta_{\text{eff}} = 0.2$.

The induced torque due to the mass accretion is $N_{\text{acc}} \approx \dot{M} \sqrt{GM_{\text{NS}} R_M}$. The total torque can be expressed in the form of $N_{\text{tot}} = n(\omega_{\text{fast}}) N_{\text{acc}}$ where $n(\omega_{\text{fast}})$ is a dimensionless function that accounts for the coupling of the magnetic field lines to the accretion disc and takes the value $\approx 7/6$ for slow rotators (for more details see Wang 1995; Parfrey, Spitkovsky & Beloborodov 2016). The spin-up rate of the NS is then given by:

$$\dot{\nu} = \frac{n(\omega_{\text{fast}})}{2\pi I_{\text{NS}}} \dot{M} \sqrt{GM_{\text{NS}} R_M}, \quad (6)$$

where $I_{\text{NS}} \simeq (1-1.7) \times 10^{45}$ g cm² is the moment of inertia of the NS (e.g. Steiner et al. 2015).

For an almost constant mass accretion rate (within a factor of ~ 2), the standard torque model can explain the NS spin period evolution for the entire period prior to MJD 58300 (Vasilopoulos et al. 2018), when the X-ray flux of NGC 300 ULX1 started to

⁴Note that Chashkina et al. (2019) normalize the accretion rates to $4\pi GM_{\text{NS}}/c\kappa$, which introduces a factor of 12 difference with the normalization adopted here.

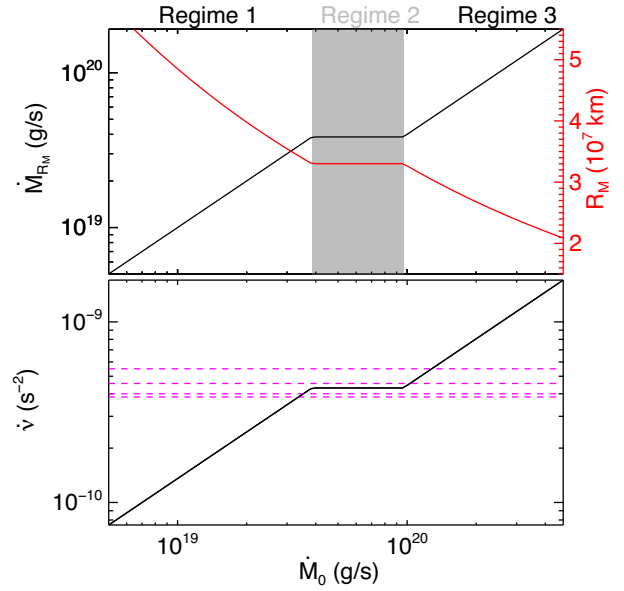


Figure 2. Top panel: Schematic dependence of the magnetospheric (inner disc) radius R_M (red line) and the mass accretion rate at that radius $\dot{M}(R_M)$ (black line) as a function of the mass accretion rate at the spherization radius \dot{M}_0 (for detailed calculations, see Chashkina et al. 2019; Mushtukov et al. 2019). The spherization (R_{sph}) and magnetospheric radii are defined by equations (3) and (7), respectively. The condition $R_{\text{sph}} = R_M$ marks the transition between regimes 1 and 2. For the definitions of the accretion regimes indicated in the plot, see Section 3. Bottom panel: Derived spin-up rate using equation (6). The horizontal lines mark the various $\dot{\nu}$ measurements based on *XMM-Newton*, *Chandra*, *NuSTAR*, and *NICER* data: 5.5×10^{-10} , 4.5×10^{-10} , 4.0×10^{-10} , and 3.8×10^{-10} s⁻² (Ray et al. 2018; Vasilopoulos et al. 2018).

Table 1. Physical parameters of NGC 300 ULX1 inferred from its spin evolution, assuming different accretion regimes.

Parameters	Regime 1 ^a	Regime 2 ^b
B (G)	6×10^{12} fixed ^c	1.4×10^{12}
$\dot{M}(R_M)$ (g s ⁻¹) ^d	2.3×10^{19}	4.0×10^{19}
R_M (km)	800	300

Notes. ^a $R_M > R_{\text{sph}}$; accretion without outflows.

^bThe mass-accretion rate at the magnetosphere is assumed constant.

^cFixed at the value derived by Vasilopoulos et al. (2018).

^dValue of an effective constant $\dot{M}(R_M)$ that would result in the observed average spin-up rate measured by the *NICER* data.

decline. Observations of NGC 300 ULX1 performed by *XMM-Newton*, *NuSTAR*, and *Chandra* have been used to determine the system's L_X and $\dot{\nu}$ at different epochs, thus allowing the estimation of the NS magnetic field, which was found to be $B \simeq 6 \times 10^{12}$ G (Vasilopoulos et al. 2018). Upon inserting the average spin-up rate for NGC 300 ULX1 as inferred by the fit to the *NICER* data ($\dot{\nu} = 4.031 \times 10^{-10}$ s⁻²) into equations (5) and (6) and setting $\xi = 0.5$, $n(\omega_{\text{fast}}) = 7/6$, $m_1 = 1.4$ and $I_{\text{NS},45} = 1.3$, we find $R_M \simeq 800$ km and $\dot{M}(R_M) \simeq 2.3 \times 10^{19}$ g s⁻¹ (see first column in Table 1).

We next explored if the same model can reproduce the spin-evolution of the NS for the 100 d period during which the observed F_X rapidly decayed and recovered (see grey shaded region in Fig. 1). For this purpose, we solved equation (6) assuming a constant magnetic field strength of $B = 6 \times 10^{12}$ G and a radiative efficiency of $\eta_{\text{eff}} = 0.2$. We performed our calculations for (i) various constant

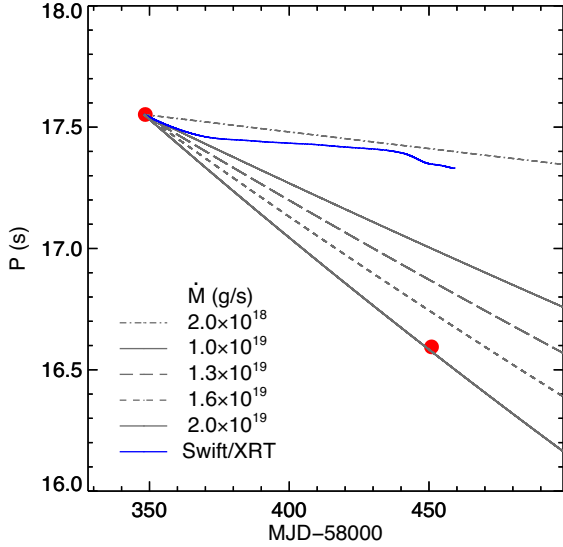


Figure 3. Predicted evolution of NS spin period P based on the Wang (1995) model for various accretion rates marked on the plot. Two red points mark the measured spin period from the *NICER* observations, as shown also in the lower panel of Fig. 1. The black lines denote the evolution of P after the *NICER* measurement (first red point) for different constant accretion rates (at R_M) marked on the plot. The evolutionary track predicted for a variable \dot{M} that follows the observed *Swift*/XRT count rate (shaded area in upper panel of Fig. 1) is plotted with a solid blue line. This solution is obtained using the best fit spectral model of Carpano et al. (2018) with no changes in absorption and $\eta_{\text{eff}} = 0.2$.

values of the accretion rate (or equivalently intrinsic L_X) and (ii) a variable accretion rate that best describes the observed temporal evolution of F_X , assuming no correction due to obscuration or extreme absorption. The derived spin-period evolutionary tracks for the two cases are plotted in Fig. 3. It is clear that the observed spin evolution does not match the one predicted for a variable mass accretion rate that matches the observed rapid decay of the X-ray flux (solid blue line). On the contrary, the observed spin evolution demands a constant super-Eddington accretion rate ($\dot{M} \simeq 1.6 \times 10^{19} \text{ g s}^{-1}$) that translates to an absorption-corrected luminosity $L_X \sim 3 \times 10^{39} \text{ erg s}^{-1}$, in agreement with the findings of Vasilopoulos et al. (2018).

3.2 Spin-evolution with outflows

Here, we expand the calculations for the spin evolution of NGC 300 ULX1 presented by Vasilopoulos et al. (2018) by taking into account the effects of outflows expected during super-Eddington accretion (Shakura & Sunyaev 1973). A major difference of the following analysis with that presented in Section 3.1, is that (under certain conditions) one can estimate the unknown parameters of the system (R_M , B , $\dot{M}(R_M)$) from just one observable (i.e. the spin-up rate $\dot{\nu}$).

Equation (3) suggests that if \dot{m}_0 is sufficiently high so that $R_{\text{sph}} > R_M$, by further increasing \dot{m}_0 , both R_M and $\dot{M}(R_M)$ remain constant and all the excess mass is lost through outflows (Lipunov 1982). These arguments have provided the baseline for the recent study of King et al. (2017), where it was shown that by just measuring the spin-up rate of the NS in ULXPs one can estimate B , R_M , and $\dot{M}(R_M)$, without any knowledge of its actual X-ray luminosity (see Section 3.1 for comparison). Using equations (3), (4), (5), and (6)

we obtain R_M , B , and $\dot{M}(R_M)$:

$$R_M \simeq 119 m_1^{-1/3} I_{\text{NS},45}^{2/3} \dot{\nu}_{-10}^{2/3} [n(\omega_{\text{fast}})]^{-2/3} \text{ km} \quad (7)$$

$$B \simeq 3.9 \times 10^{10} \xi^{-7/4} m_1^{-1/2} R_{\text{NS},6}^{-3} I_{\text{NS},45}^{3/2} \dot{\nu}_{-10}^{3/2} [n(\omega_{\text{fast}})]^{-3/2} \text{ G} \quad (8)$$

$$\dot{M}(R_M) \simeq 1.6 \times 10^{19} m_1^{-1/3} I_{\text{NS},45}^{2/3} \dot{\nu}_{-10}^{2/3} [n(\omega_{\text{fast}})]^{-2/3} \text{ g s}^{-1}, \quad (9)$$

where $R_{\text{NS},6} \equiv R_{\text{NS}}/10^6 \text{ cm}$, $\dot{\nu}_{-10} \equiv \dot{\nu}/10^{-10} \text{ s}^{-2}$ and $I_{\text{NS},45} \equiv I_{\text{NS}}/10^{45} \text{ g cm}^2$. By inserting the average spin-up rate for NGC 300 ULX1 as inferred by the fit to the *NICER* data ($\dot{\nu} = 4.031 \times 10^{-10} \text{ s}^{-2}$) into equations (7)–(9) and setting $\xi = 0.5$, $n(\omega_{\text{fast}}) = 7/6$, $m_1 = 1.4$, and $I_{\text{NS},45} = 1.3$, we find $B \simeq 1.4 \times 10^{12} \text{ G}$, $R_M \simeq 300 \text{ km}$, and $\dot{M}(R_M) \simeq 4 \times 10^{19} \text{ g s}^{-1}$ (see second column in Table 1). For these parameters, the inner disc is expected to be radiation-pressure dominated (see e.g. fig. 7 in Mönkkönen et al. 2019).

We can also compute the luminosity that would be released as the mass reaching R_M is accreted onto the NS by adopting the value of $\dot{M}(R_M)$ we derived above. This yields an isotropic X-ray luminosity of $6.6 \times 10^{39} \text{ erg s}^{-1}$ (for $\eta_{\text{eff}} = 0.2$), which is a factor of 2 higher than the observed luminosity attributed to the pulsating hard component of the X-ray spectrum in NGC 300 ULX1 (Carpano et al. 2018; Koliopoulos et al. 2019). Unless the radiative efficiency is much lower than 10 per cent – 20 per cent, no beaming is needed to explain the spectral and temporal properties of NGC 300 ULX1.

Using the derived value of R_M and the condition $R_{\text{sph}} > R_M$, we can derive a lower limit on the mass accretion rate at the spherization radius, i.e. $\dot{m}_0 \gtrsim 14$. We can also place a rough upper limit on \dot{m}_0 by noting that $\dot{\nu}$ does not vary much (see Fig. 1), suggesting an approximately constant accretion rate at the magnetospheric radius. The latter condition can be realized only for a narrow range of super-Eddington accretion rates (for a schematic illustration see grey-shaded region in the top panel of Fig. 2). This range of accretion rates was found to be only weakly dependent on the magnetic field strength of the NS (see fig. 12–13 in Chashkina et al. 2019). Beyond this range, the time-derivative of the NS spin frequency is expected to depend more strongly on the accretion rate, as schematically shown in the bottom panel of Fig. 2. This statement is true regardless of the specific dependence of R_M on \dot{m}_0 (see e.g. fig. 12 in Chashkina et al. 2019), which is determined by the interplay of mass-loss through outflows and advection of heat in the inner disc and is model-dependent. As the long-term spin evolution of NGC 300 ULX1 is consistent with an almost constant $\dot{\nu}$ (see Fig. 1), we can place a rough upper limit on the accretion rate at the spherization radius, i.e. $\dot{m}_0 \lesssim 50$ for $B \sim 10^{12} \text{ G}$.

4 ON THE ORIGIN OF THE OBSCURING MATERIAL

We have demonstrated that the NS continues to spin up with an almost constant $\dot{\nu}$ during the period of decreasing flux (MJD 58350–58450), suggesting an almost constant accretion rate at the NS magnetospheric radius. Thus, the decrease of the observed X-ray flux cannot be intrinsic to the source but it can rather be caused by absorption.

Radiatively driven outflows launched from the disc can be optically thick to the hard radiation produced by the NS, acting effectively as obscuring envelopes (e.g. Poutanen et al. 2007; Abolmasov, Karpov & Kotani 2009). However, radiation can still

escape from a central conical region (with opening angle θ_c) that is devoid of obscuring material (Poutanen et al. 2007). For a radiation-pressure-dominated accretion disc, truncated at $R_M < R_{\text{sph}}$, the mass outflow rate up to a radius R , lying within the spherization radius, can be estimated by:

$$\dot{M}_{\text{out}}(R) = \int_{R_M}^R dR' \frac{d\dot{M}(R')}{dR'} \approx \dot{m}_0 \dot{M}_{\text{Edd}} \frac{R - R_M}{R_{\text{sph}}}, \quad (10)$$

where equation (4) was used. Following Poutanen et al. (2007) (see equations 27, 28, and 30 therein), we calculate the maximum Thomson optical depths in the directions perpendicular ($\tau_{\perp, \text{max}}$) and parallel ($\tau_{\parallel, \text{max}}$) to the accretion disc plane:

$$\tau_{\perp, \text{max}} = \frac{\tau_0 \dot{m}_0}{\beta r_{\text{sph}}} \left(\sqrt{r_{\text{sph}}} - \frac{r_M}{\sqrt{r_{\text{sph}}}} \right) \quad (11)$$

$$\tau_{\parallel, \text{max}} = \frac{\tau_0 \dot{m}_0}{\beta \cot \theta_c r_{\text{sph}}} \left[2 \left(\sqrt{r_{\text{sph}}} - \sqrt{r_M} \right) + 2r_M \left(r_{\text{sph}}^{-1/2} - r_M^{-1/2} \right) + \sqrt{r_{\text{sph}}} \left(1 - \frac{r_M}{r_{\text{sph}}} \right) \right], \quad (12)$$

where $\beta \sim 1$ is the ratio of the outflow speed to the Keplerian velocity at R_{sph} , $\theta_c \sim \pi/4$, $\tau_0 \equiv \sqrt{6\kappa} \dot{M}_{\text{Edd}} / 4\pi c R_0$, $R_0 = 6GM_{\text{NS}}/c^2$, and $r \equiv R/R_0$. For $R_M = 300$ km (see Table 1) and $\dot{m}_0 \gtrsim 20$, we find $\tau_{\parallel, \text{max}} \approx \tau_{\perp, \text{max}} \gtrsim 5$. This corresponds to a maximum column density $N_{\text{H}} \gtrsim 7.5 \times 10^{24} \text{ cm}^{-2}$ for a line-of-sight cutting through the outflow, and it is sufficient to explain the X-ray flux decay due to absorption (see also Carpano et al. 2018).

The accretion disc around a black hole or a NS can precess due to the Lense–Thirring effect (Bardeen & Petterson 1975; Truemper et al. 1986). Recently, it has been postulated that this mechanism can explain the superorbital modulation in the observed flux of ULXPs (Middleton et al. 2018). According to this scenario, the drop in the observed flux is due to changes in the geometrical configuration of the inner accretion disc and the outflow. Thus, in ULXPs the observer can only see the NS when the wind-free region of the outflow aims directly at him/her. The time-scale of the outflow precession is (see equation 5 of Middleton et al. 2018):

$$P_{\text{prec}} \approx P_{\text{NS}} \frac{R_{\text{sph}}^3 c^2}{6GI_{\text{NS}}} \frac{1 - (R_M/R_{\text{sph}})^3}{\ln(R_{\text{sph}}/R_M)} \left(\frac{R_{\text{out}}}{R_{\text{sph}}} \right)^2, \quad (13)$$

where R_{out} is the radius at which the precession of the outflow ceases. An upper limit on the precession period can be derived if $R_{\text{out}} \sim R_{\text{ph}}$, where the photospheric radius R_{ph} is estimated by the condition $\tau_{\perp} = 1$:

$$R_{\text{ph}} \approx \frac{\tau_0 \dot{m}_0 R_0}{\beta \sqrt{r_{\text{sph}}}} (r_{\text{sph}} - r_M). \quad (14)$$

For $\beta \sim 1$, $R_M = 300$ km, and $\dot{m}_0 = 20$ (50), we obtain $R_{\text{ph}} \simeq 2000$ km (2×10^4 km). Similar values of the photospheric radius can be obtained by requiring $\tau_{\parallel} = 1$, if $\theta_c \sim \pi/4$. We note that other opening angles lead to non-spherical photospheres by introducing a dependence of R_{ph} on θ_c . Any information about changes in the inflow due to the Lense–Thirring torque must be communicated to all parts of the outflow within the photosphere, for it to precess out to that radius. It is possible, however, that the outflow becomes supersonic at $R \ll R_{\text{ph}}$, thus becoming decoupled from the inflow. A lower limit on the predicted precession period can be derived, if the outflow remains subsonic within the spherization radius. In this case, $R_{\text{out}} \gtrsim R_{\text{sph}}$. An accurate calculation of P_{prec} requires detailed knowledge of the outflow thermodynamical properties and geometry (i.e. density and pressure radial profile,

opening angle) and, as such, lies beyond the scope of this paper (see also Middleton et al. 2019).

Assuming that the observed X-ray flux decay is associated with Lense–Thirring precession, the corresponding period should be longer than a year, since we have only observed one such event within one year of continuous monitoring. For the current spin period $P_{\text{NS}} = 16$ s, $R_M = 300$ km, and $\dot{m}_0 = 20$ (50) we find⁵ $P_{\text{prec}} \simeq 2.3$ yr (300 yr), if $R_{\text{out}} = R_{\text{ph}}$ and $P_{\text{prec}} \simeq 0.4$ yr (3.0 yr), if $R_{\text{out}} = 2R_{\text{sph}}$. As the spin-up of the NS continues, shorter P_{prec} are expected. Due to the strong dependence of P_{prec} on \dot{m}_0 , we can place upper limits on the latter by detecting future periodic dips in the X-ray flux due to precession. Future monitoring observations could provide crucial insights on this phenomenon.

5 CONCLUSIONS

We have analysed monitoring observations of NGC 300 ULX1 obtained with *Swift*/XRT within 2018, and presented an updated X-ray light-curve. We showed that within a 100 d period the observed flux of the system rapidly decayed. Moreover, we triggered *NICER* target of opportunity observations to follow the spin evolution on the NS during the low-flux epoch. We showed that the NS of NGC 300 ULX1 continues to spin up with a rate that translates to a constant mass accretion rate within 2018, even at epochs where the observed flux dropped by a factor of ~ 50 . We interpreted the changes in the observed flux as a result of increased absorption and obscuration. Outflows from a radiation-dominated accretion disc can provide an optically thick structure that could be responsible for the increased absorption. In this regime, the observed L_X underpredicts the mass accretion rate assuming typical radiative efficiency for the accretion column, thus no strong beaming (if any) is needed to explain the observed super-Eddington luminosity. Based on the inferred properties of NGC 300 ULX1 we expect the orientation of the outflows to change on year-long time-scales due to Lense–Thirring precession. The detection of multiple (quasi-periodic) dips in the X-ray flux within the next decade will provide a firm confirmation for the Lense–Thirring precession being the mechanism responsible for the X-ray obscuration.

ACKNOWLEDGEMENTS

The authors would like to thank the anonymous referee for their constructive review. GV would like to thank D. Walton, F. Fürst, M. Bachetti, and M. Heida for discussions on NGC 300 ULX1 that took place at the 17th High Energy Astrophysics Division (HEAD17) meeting. MP acknowledges support from the Lyman Jr. Spitzer Postdoctoral Fellowship and Fermi Guest Investigator grant 80NSSC18K1745. Neutron Star Interior Composition Explorer (NICER) work at U. S. Naval Research Laboratory (NRL) is funded by the National Aeronautics and Space Administration (NASA). We thank Z. Arzoumanian and the NICER team for their help and assistance during the execution of the NICER ToO observations. We acknowledge the use of public data from the Neil Gehrels *Swift* Observatory data archive.

⁵This calculation is just introduced as an order of magnitude estimation. For a discussion about the uncertainties, we point the reader to Middleton et al. (2018, 2019).

REFERENCES

- Abolmasov P., Karpov S., Kotani T., 2009, *PASJ*, 61, 213
- Bachetti M. et al., 2014, *Nature*, 514, 202
- Bardeen J. M., Petterson J. A., 1975, *ApJ*, 195, L65
- Becker P. A., Wolff M. T., 2007, *ApJ*, 654, 435
- Binder B., Williams B. F., Kong A. K. H., Gaetz T. J., Plucinsky P. P., Dalcanton J. J., Weisz D. R., 2011, *ApJ*, 739, L51
- Brightman M. et al., 2019, *ApJ*, 873, 115
- Campana S., Stella L., Mereghetti S., de Martino D., 2018, *A&A*, 610, A46
- Carpano S., Haberl F., Maitra C., Vasilopoulos G., 2018, *MNRAS*, 476, L45
- Chashkina A., Lipunova G., Abolmasov P., Poutanen J., 2019, *A&A*, 626, A18
- Corbet R. H. D., 1996, *ApJ*, 457, L31
- Evans P. A. et al., 2007, *A&A*, 469, 379
- Evans P. A. et al., 2009, *MNRAS*, 397, 1177
- Fürst F., Walton D. J., Stern D., Bachetti M., Barret D., Brightman M., Harrison F. A., Rana V., 2017, *ApJ*, 834, 77
- Fürst F. et al., 2018, *A&A*, 616, A186
- Ghosh P., Lamb F. K., Pethick C. J., 1977, *ApJ*, 217, 578
- Gieren W., Pietrzyński G., Soszyński I., Bresolin F., Kudritzki R.-P., Minniti D., Storm J., 2005, *ApJ*, 628, 695
- Illarionov A. F., Sunyaev R. A., 1975, *A&A*, 39, 185
- Israel G. L. et al., 2017, *Science*, 355, 817
- Kaaret P., Simet M. G., Lang C. C., 2006, *ApJ*, 646, 174
- Kaaret P., Feng H., Roberts T. P., 2017, *ARA&A*, 55, 303
- Kelly B. C., 2007, *ApJ*, 665, 1489
- King A., Lasota J.-P., 2019, *MNRAS*, 485, 3588
- King A., Lasota J.-P., Kluźniak W., 2017, *MNRAS*, 468, L59
- King A. R., Davies M. B., Ward M. J., Fabbiano G., Elvis M., 2001, *ApJ*, 552, L109
- Koliopanos F., Vasilopoulos G., Godet O., Bachetti M., Webb N. A., Barret D., 2017, *A&A*, 608, A47
- Koliopanos F., Vasilopoulos G., Buchner J., Maitra C., Haberl F., 2019, *A&A*, 621, A118
- Leahy D. A., Darbro W., Elsner R. F., Weisskopf M. C., Sutherland P. G., Kahn S., Grindlay J. E., 1983, *ApJ*, 266, 160
- Lipunov V. M., 1982, *SvA*, 26, 54
- Middleton M. J. et al., 2018, *MNRAS*, 475, 154
- Middleton M., Fragile P. C., Ingram A., Roberts T. P., 2019, *MNRAS*, preprint ([arXiv:1905.02731](https://arxiv.org/abs/1905.02731))
- Mönkkönen J., Tsygankov S. S., Mushtukov A. A., Doroshenko V., Suleimanov V. F., Poutanen J., 2019, *A&A*, 626, A106
- Motch C., Pakull M. W., Soria R., Grisé F., Pietrzyński G., 2014, *Nature*, 514, 198
- Mushtukov A. A., Suleimanov V. F., Tsygankov S. S., Poutanen J., 2015, *MNRAS*, 454, 2539
- Mushtukov A. A., Ingram A., Middleton M., Nagirner D. I., van der Klis M., 2019, *MNRAS*, 484, 687
- Parfrey K., Spitkovsky A., Beloborodov A. M., 2016, *ApJ*, 822, 33
- Poutanen J., Lipunova G., Fabrika S., Butkevich A. G., Abolmasov P., 2007, *MNRAS*, 377, 1187
- Ray P. S. et al., 2011, *ApJS*, 194, 17
- Ray P. S. et al., 2018, *ApJ*, 879, 130
- Shakura N. I., Sunyaev R. A., 1973, *A&A*, 24, 337
- Steiner A. W., Gandolfi S., Fattoyev F. J., Newton W. G., 2015, *Phys. Rev. C*, 91, 015804
- Truemper J., Kahabka P., Oegelman H., Pietsch W., Voges W., 1986, *ApJ*, 300, L63
- Vasilopoulos G., Haberl F., Carpano S., Maitra C., 2018, *A&A*, 620, L12
- Wang Y.-M., 1995, *ApJ*, 449, L153

This paper has been typeset from a $\text{\TeX}/\text{\LaTeX}$ file prepared by the author.